



Conformational properties and photochemistry of tetrazolylpyridines in low temperature matrices. Spectroscopic evidence for the photochemical carbon-to-nitrogen rearrangement

M. Pagacz-Kostrzewa, J. Krupa, A. Olbert-Majkut, M. Podruczna, R. Bronisz, M. Wierzejewska^{*}

Faculty of Chemistry, University of Wrocław, Joliot-Curie 14, 50-383 Wrocław, Poland

ARTICLE INFO

Article history:

Received 1 June 2011

Received in revised form 4 August 2011

Accepted 22 August 2011

Available online 27 August 2011

Keywords:

Tetrazole

Photolysis

Matrix isolation

Carbon-to-nitrogen rearrangement

Infrared spectra

B3LYP calculations

ABSTRACT

The most stable conformers of 2-(tetrazol-1-yl)-, 3-(tetrazol-1-yl)- and 2-(tetrazol-5-yl)pyridines undergo photolysis in Ar matrices at cryogenic temperatures to yield pyridin-2-ylcarbodiimide or pyridin-3-ylcarbodiimide. Spectroscopic evidence of carbon-to-nitrogen rearrangement in the case of the 2-(tetrazol-5-yl)pyridine molecule is provided. For the latter molecule a second pathway leads to the 1-cyclopenta-2,4-dienylketenimine formation. The experimental findings are supported by extensive B3LYP/6-311++G(2d,2p) calculations.

© 2011 Elsevier Ltd. All rights reserved.

1. Introduction

There is a continuous interest in tetrazole derivatives due to their possible applications as ligands in coordination chemistry,¹ high energy materials² and biologically active compounds.³ 5-Substituted tetrazoles were found to be useful as a bioisosteric replacement for the carboxylic acid moiety,⁴ while 1,5-disubstituted tetrazole ring is known to be an excellent mimic of the *cis*-amide bond.⁵ Tetrazole derivatives are also very stimulating heterocycles from an academic viewpoint due to their tautomeric and conformational properties^{6–9} and very interesting photochemistry.^{6–8,10–13} The title compounds: 2-(tetrazol-1-yl)pyridine (P2T), 3-(tetrazol-1-yl)pyridine (P3T) and 2-(tetrazol-5-yl)pyridine (PT), although relatively simple, are much less frequently studied tetrazole derivatives. The two former do not contain a H-atom attached to the tetrazole N atom, and the expected conformers should differ by the relative pyridine and tetrazole rings arrangement. In turn, the tetrazole ring in PT is attached to the pyridine ring through the carbon atom, and this molecule possesses an N–H component. For the latter molecule both structural conformers and different annular tautomers are expected to exist. To the best of our knowledge neither of the title compounds has been the subject of spectroscopic or theoretical investigations, although a crystal

structure of P2T was reported in two papers.^{14,15} The P2T molecule was found to be almost perfectly flat with the pyridine nitrogen *syn*-orientated to the tetrazole C–H group. Such an arrangement is favoured due to the vicinity of the H atom and the pyridine N lone pair. P2T takes part in three intermolecular C–H...N hydrogen bonds in the crystal, forming a novel 2-D network.¹⁵ X-ray studies were also performed for PT. This compound crystallizes as the more common C-aryl-NH-tetrazole form with the H atom attached to the N1 atom of the tetrazole ring.¹⁵ The pyridyl and tetrazolyl rings are almost coplanar, and in contrast to P2T the pyridyl N atom and tetrazolyl N–H group, are *transoid* to each other.¹⁵

Photochemistry of the tetrazole derivatives has been the subject of intensive studies. The photolysis of the unsubstituted tetrazole was studied in an argon matrix by Maier et al.¹⁰ and allowed the spectroscopic identification of a number of photoproducts, such as nitrilimine HCNNH or carbodiimide HNCNH. Depending on the nature and position of the substituents, the tetrazole derivatives may photolyse through different pathways forming diverse products.^{7,12,13,16–20}

All three subjects in the present study are structural isomers. 2-(Tetrazol-1-yl)pyridine (P2T) and 3-(tetrazol-1-yl)pyridine (P3T) are positional isomers, and 2-(tetrazol-5-yl)pyridine (PT) is a functional group isomer of P2T. The aim of this work was the experimental characterization of the conformers of P2T, P3T and PT isolated in solidified argon by means of matrix isolation and FTIR spectroscopy. A second objective was to study UV-induced

^{*} Corresponding author. Tel.: +4871 3757332; fax: +4871 3282348; e-mail address: maria.wierzejewska@chem.uni.wroc.pl (M. Wierzejewska).

photochemistry of these compounds with special emphasis on the possible impact of the structural isomerism of the compounds on the available photolysis pathways. Interpretation of the experimental finding was supported by extensive DFT and TD-DFT calculations for the ground and excited singlet states.

2. Results and discussion

2.1. Structure and energetics of the minima on the S_0 potential energy surface

2.1.1. 2-(Tetrazol-1-yl)pyridine (P2T) and 3-(Tetrazol-1-yl)pyridine (P3T). Both P2T and P3T species have one internal rotation axis that give rise to two different conformational isomers denoted as P2Ta, P2Tb and P3Ta, P3Tb, respectively. All four stable P2T and P3T structures optimized at the B3LYP/6-311++G(2d,2p) level are presented in Fig. 1 together with the adopted numbering schemes. The geometry of the calculated species is given in Table S1 in the Supplementary data. The energetic parameters including: relative energies, relative Gibbs free energies, abundances at 298 K and at the sublimation temperature calculated for P2T and P3T conformers are gathered in Table S2 in the Supplementary data. The P2Ta, P2Tb and P3Ta, P3Tb species differ in the mutual orientation of the pyridine and tetrazole rings: the N9C8N1C5 angle for P2T and the C8C7N1C5 angle for P3T are also given in this table. For both P2T and P3T molecules the more stable among the two isomers is that with the pyridine nitrogen *syn*-oriented to the tetrazole C–H group. In the case of P2T the *syn* configuration is clearly favourable as compared with the *trans*-orientation because of the vicinity of the tetrazole H atom and the pyridine N lone pair. Such close C–H...N contact determines the stability of P2Ta that is 22.94 kJ mol^{−1} lower in energy than the second P2Tb species and leads to the 100% population of the former conformer. The calculated P2Ta geometry is consistent with that determined experimentally by X-ray diffraction^{14,15} in the P2T crystal. In turn, for the P3T molecule one cannot expect any spatial vicinity of tetrazole H atom and pyridine N atom for the *syn*-conformer and accordingly both P3Ta and P3Tb are similar in energy and characterized by a small difference in their stability of 2.63 kJ mol^{−1}. The calculated abundance of the P3Ta and P3Tb conformers equals 73.85% and 26.15% at 298 K and it changes very slightly at the experimental sublimation temperature of 333 K (73.77% and 26.23%).

2.1.2. 2-(Tetrazol-5-yl)pyridine (PT). PT may exist in two tautomeric forms differing by the position of the H atom in the tetrazolyl ring. For both PT tautomers two conformers may exist with different arrangement of the two rings in the molecule giving altogether four stable forms. These structures are presented in Fig. 2 and their geometry is given in Table S1. The most stable PT1a form with the H atom connected to the N1 atom of the tetrazolyl ring is stabilized by the favourable interaction of this hydrogen with the N9 atom of the pyridine ring. The next structure in order of stability PT2a with the H-atom connected to N2 of the tetrazolyl ring is 13.90 kJ mol^{−1} higher in energy than the most stable PT structure. As can be seen in Fig. 2 PT1a and PT2a structures have their higher energy counterparts with a different orientation of the tetrazolyl ring relative to the pyridine moiety (PT1b and PT2b). The calculations revealed also the existence of two higher energy conformers (PT3a, PT3b). These species are characterized by the sp³ hybridization state of the C5 atom of the tetrazole moiety leading to the loss of the tetrazole ring aromaticity and resulting in a decrease in their stability (see Table S2). The geometry of the two latter species as well as that obtained for all stable PT minima is given in the Supplementary data (Fig. S1, Table S1). According to the calculations 98.56% of PT molecules are expected to appear at the temperature of

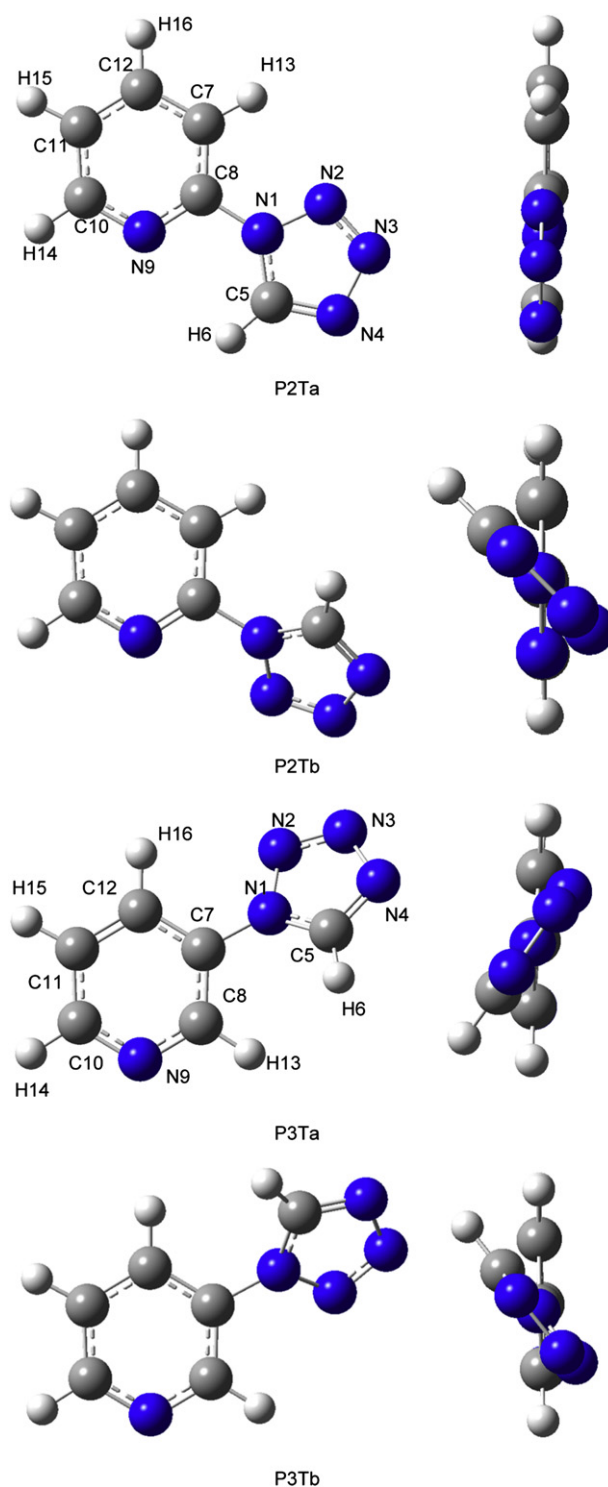


Fig. 1. B3LYP/6-311++G(2d,2p) optimized structures of the P2T and P3T conformers.

sublimation (340 K) as the most stable PT1a tautomer while the remaining species have a total population of 1.44% and are not of importance in relation to the experimental spectra.

2.2. Structure of the transition states and conformational interconversion barriers on the S_0 potential energy surface

All transition states (TS) connecting the P2T, P3T and PT minima have been located on the corresponding potential energy surfaces

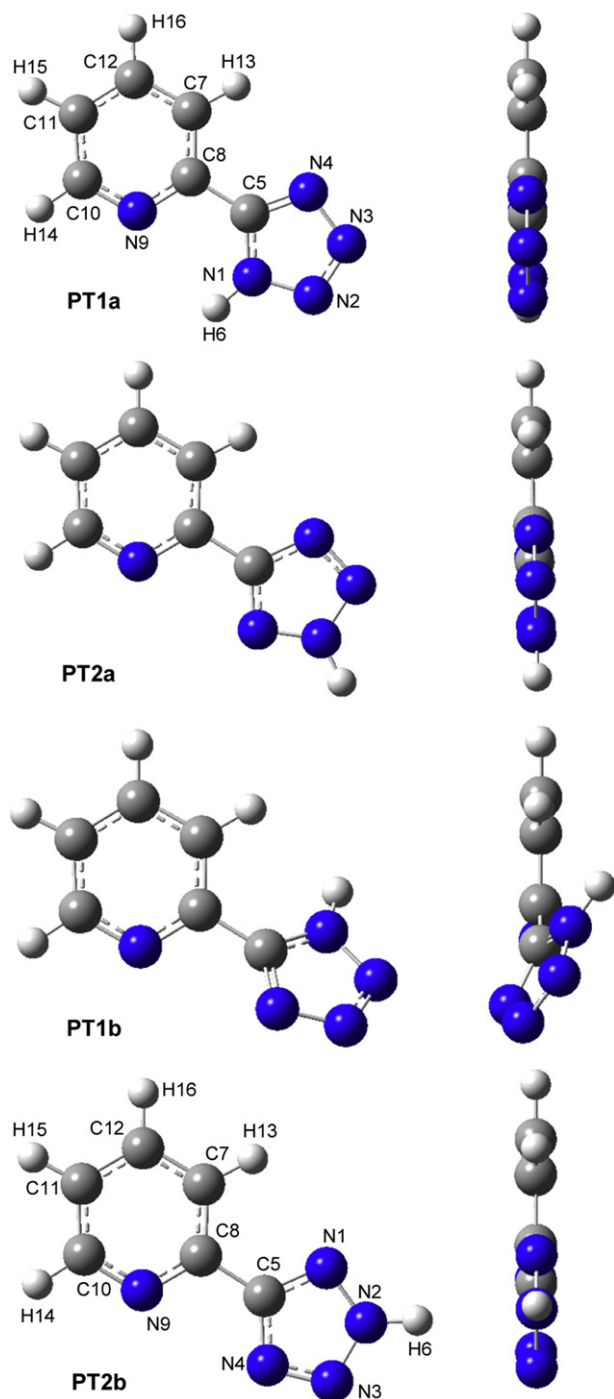


Fig. 2. B3LYP/6-311++G(2d,2p) optimized structures of the PT isomers.

in the aim to estimate the energy barriers between different P2T, P3T or PT species. Fig. 3 shows the B3LYP/6-311++G(2d,2p) optimized structures of the TS1 and TS2 transition states linking P2Ta with P2Tb and P3Ta with P3Tb, respectively, while five transition states (TS3–TS7) that connect four PT species are given in Fig. S2 in the Supplementary data. The related energetics for these transition states and their imaginary frequency values are gathered in Table S2 and the respective ZPE corrected potential energy diagrams are presented in Figs. 4 and 5. The most stable P2Ta and P3Ta conformers may isomerize through TS1 and TS2, to form P2Tb and P3Tb, respectively. The corresponding energy barriers for the P2Ta→P2Tb and P3Ta→P3Tb transformations are very much different and are 24.14 and 6.12 kJ mol^{−1}, respectively. The TS1

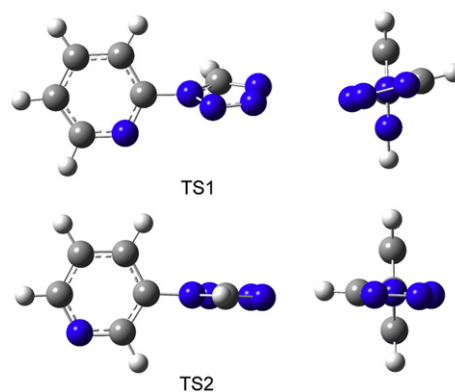


Fig. 3. B3LYP/6-311++G(2d,2p) optimized structures of the transition states linking P2T and P3T conformers.

transition state is characterized by the intermediate N9C8N1C5 angle of -77.1° as compared to those calculated for P2Ta and P2Tb (-0.1 and -136.0 , respectively). Similarly, the TS2 transition state has the C8C7N1C5 angle equal to -93.7° that is intermediate between -32.9° and -142.6° found for the P3Ta and P3Tb minima, respectively.

Three of the five transition states located on the PT potential energy surface (T3, T4 and T5) are characterized by very high energies of more than 220 kJ mol^{−1}. TS3, TS4 and TS5 are transition states for the 1,2-hydrogen transfer reactions appearing between PT1a↔PT2a, PT2a↔PT2b and PT1b↔PT2b. In turn, much lower energy barriers were found for the PT2a↔PT2b and PT1a↔PT1b interconversions consisting of rotation of the tetrazolyl ring relative to the pyridine moiety (see Table S2 and Fig. 5).

2.3. Changes of structural parameters and charge distribution of P2Ta, P3Ta and PT1a in their S₁ excited states. TD-DFT calculations

Optimization of the P2Ta, P3Ta and PT1a species in both S₀ and S₁ states using DFT and TD-DFT methods, respectively, reveals quite

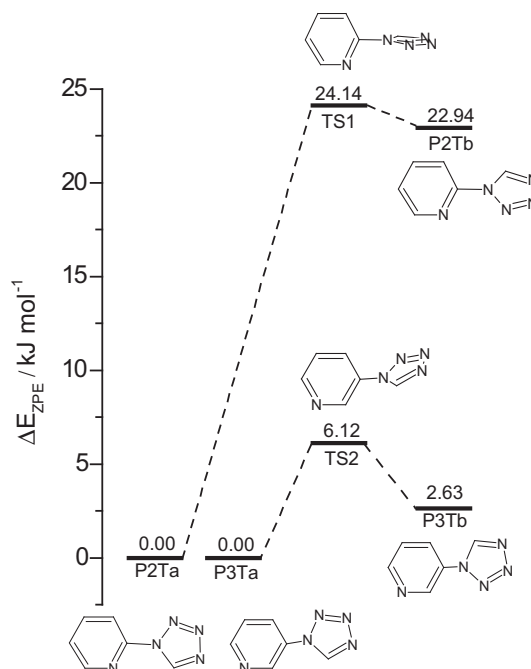


Fig. 4. B3LYP/6-311++G(2d,2p) ZPE corrected potential energy diagram for P2T and P3T isomerizations.

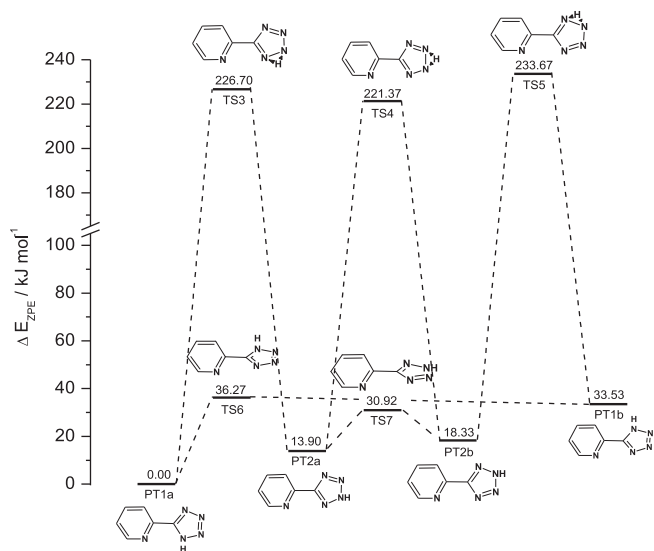


Fig. 5. B3LYP/6-311++G(2d,2p) ZPE corrected potential energy diagram for PT isomerizations.

meaningful changes in the geometry of the S_1 excited states as compared to the corresponding S_0 states. These data are gathered in Table S3 in the Supplementary data. From the comparison of the S_0 and S_1 geometries presented in Table S3 it is clear that P3Ta becomes planar upon excitation as evidenced by the calculated values of the C8C7N1C5 dihedral angle of -26.0° and -0.1° in S_0 and S_1 , respectively. In turn, P2Ta and PT1a, which are planar in the ground state remain flat in the S_1 state. Pronounced changes in the bond distances and angle values are observed upon excitation within both pyridine and tetrazole rings. Fig. 6 displays the electron density difference plots between the densities of $S_1(A')$ and $S_2(A')$ and the density of the ground state for the P2Ta species. Analogous figures obtained for the P3Ta and PT1a molecules are presented in Fig. S3 in the Supplementary data. From Fig. 6 it is seen that both excited states are delocalized on both rings present in the molecule. The corresponding calculated energy of the $S_1 \leftarrow S_0$ and $S_2 \leftarrow S_0$ transitions equals to 245.2 and 228.0 nm and the oscillator strengths amount to 0.171 and 0.201, respectively.

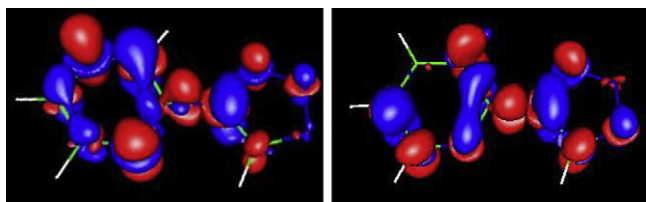


Fig. 6. Density differences calculated at the P2Ta ground state, between S_1 and S_0 (left) and S_2 and S_0 (right). The red isosurface represents a value of 0.002 and the blue one a value of -0.002 . Upon excitation the electron density moves from blue to red regions.

2.4. Matrix isolation infrared spectra of P2T, P3T and PT in solid argon and their comparison to the theoretical predictions

According to the estimated gas phase abundance for the P2T and PT species (see Table S2) only the most stable structures, namely P2Ta and PT1a are expected to be present in P2T/Ar and PT/Ar matrices, respectively. Fig. 7 shows the infrared spectra of the as-deposited P2T/Ar (black trace, upper part) and PT/Ar (red trace, upper part) matrices as well as a simulated spectra of the P2Ta and PT1a species. In agreement with the expectations, only the most stable P2Ta and PT1a species were found in the P2T/Ar and PT/Ar

matrices, respectively. It is demonstrated in Fig. 7 by good accordance between the experimental infrared spectra obtained for P2T/Ar and PT/Ar and those calculated for the most stable P2Ta and PT1a structures.

Fig. 8 (upper trace) shows the infrared spectrum of the as-deposited P3T/Ar matrix at 15 K. Closer inspection of this spectrum reveals that both P3Ta and P3Tb conformers are present in the matrices. Indeed, a satisfying reproduction of the experimental data was obtained when P3Ta and P3Tb conformers were taken into account with the population equal to that estimated from the gas phase equilibrium at the sublimation temperature 333 K. The sum spectrum obtained by adding the B3LYP/6-311++G(2d,2p) spectra of P3Ta and P3Tb weighted by their respective abundances (73.77% and 26.23%) is presented for comparison in Fig. 8 (middle trace).

Table S4 in the Supplementary data summarizes the positions of the bands observed in the experimental spectra together with the corresponding theoretical data and results of potential energy distribution (PED) calculations for the P2T, P3T and PT species. The proposed assignment of the IR bands, also included in Table S4, is based on the analysis of the theoretically predicted spectra and the potential energy distribution (PED) matrixes obtained for the studied compounds.

2.5. Broad-band UV-irradiation experiments

The photochemistry of all three compounds was studied and the resulting photochemical processes were followed by IR spectroscopy. Upon broad-band UV-irradiation, the bands due to the substrate molecules decreased in intensity and simultaneously new features appeared in the spectra. The interpretation of the experimental data was supported by the B3LYP/6-311++G(2d,2p) calculations of the possible photoproducts and based on, whenever available, previously reported infrared spectra of putative photoproducts.

Matrices containing P2T, P3T or PT species were subjected to the broad-band irradiation with the UV optical filters to determine the threshold energy for the photolytic reactions occurring in the studied matrices. It appeared that for both P2T and P3T there was no observable photolysis unless radiation with $\lambda \leq 280$ nm was used while for PT the photolysis started at $\lambda \leq 305$ nm. The detected variation in the threshold energy is qualitatively consistent with the results of the performed TD-DFT calculations. The estimated HOMO-LUMO energy gap for the P2Ta, P3Ta and PT1a species equals 245, 242 and 252 nm, respectively, with the relatively high oscillator strength for the corresponding electronic transitions of 0.1711, 0.1116 and 0.2500.

Further on, the P2T/Ar, P3T/Ar and PT/Ar matrices were irradiated with the full output of the high pressure Xe lamp and these results are discussed below.

2.5.1. P2T/Ar photolysis. Upon irradiation of the P2T/Ar matrices (only P2Ta conformer present) using the full output of the Xe lamp, the most intense photoproducts bands were found in the 2200–2100 cm^{-1} spectral region, that is, characteristic of C=N stretching mode. New bands were observed also in the 3450–3400 cm^{-1} range due to the N–H group stretching vibration. The apparent changes were noticeable in the 1640–1550 cm^{-1} region. The results are presented in Fig. 9A, where representative portions of the P2T/Ar difference spectra before and after photolysis are shown together with the appropriate calculated spectra for precursor and product molecules. Three spectral features appearing between 3440–3400 cm^{-1} separated by 8–10 wavenumbers are assigned, on the basis of the annealing experiment performed after photolysis, to one product P1, whose structure will be revealed later in this paper, trapped in different matrix sites. When the

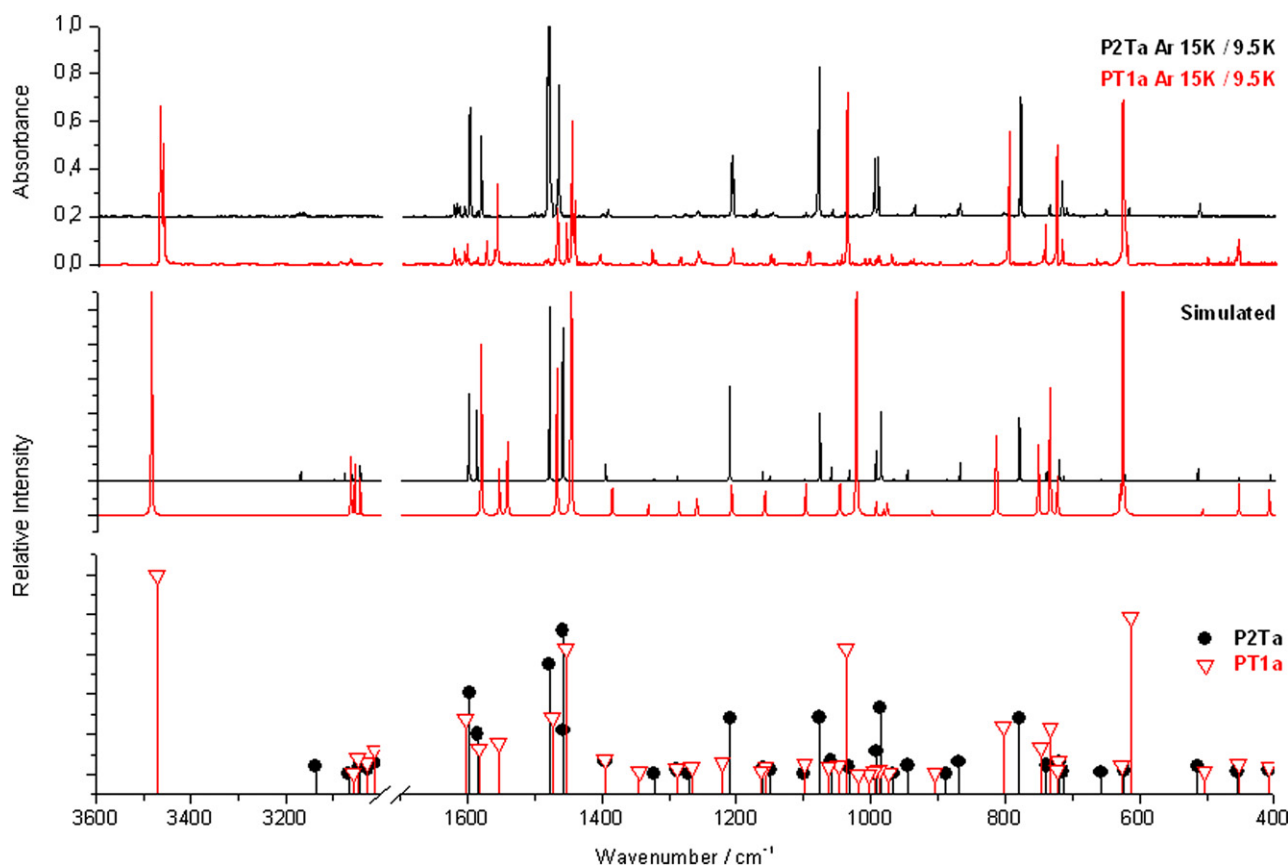


Fig. 7. Infrared spectra of P2Ta and PT1a: *top frame*: spectrum of P2Ta isolated in Ar matrix (black line) and spectrum of PT1a isolated in Ar matrix (red line), deposition at 15 K, measurement at 9.5 K; *middle frame*: B3LYP/6-311++G(2d,2p) simulated spectra of P2Ta (black) and PT1a (red) created using Lorentzian functions centred at the calculated frequencies scaled as described in Section 4.2 and with the bandwidth-at-half-height equal to 0.5 cm^{-1} . *bottom frame*: calculated spectra of P2Ta (black) and PT1a (red) scaled by the same scaling factors as for the middle frame.

temperature was kept at 28 K for 15 min, the intensity of the band at 3423.0 cm^{-1} increased at the expense of two other features in this region (3430.5 and 3412.5 cm^{-1}). Similar behaviour was observed in the $2200\text{--}2100\text{ cm}^{-1}$ region where the intensity of two weaker bands at 2143.0 and 2133.5 decreased on annealing with the simultaneous growth of the most intense absorption at 2130.0 cm^{-1} .

2.5.2. P3T/Ar photolysis. The broad-band UV irradiation of P3T/Ar matrices (two P3Ta and P3Tb conformers present) led to the simultaneous decrease in the area of the P3Ta and P3Tb bands and appearance of new product bands. The overall picture after photolysis of the P3T/Ar is analogous to that described for the P2T/Ar matrices. A similar set of product bands is observed with the maxima slightly shifted as compared to the P1 product (see Fig. 9B) and new bands appearing in the P3T/Ar spectra after photolysis are assigned to the product P2.

2.5.3. PT/Ar photolysis. When the PT/Ar matrices (one PT1a conformer present) were subjected to the broad-band UV irradiation, the decrease of the precursor absorptions is accompanied by appearance of two sets of bands attributed to two different photolysis products. The bands belonging to the first set are exactly the same, both in position and shape, as those observed for the P1 product appearing after P2Ta photolysis (see Fig. 9C). The second set consists of 17 spectral features with the strongest band situated at 2045.5 cm^{-1} . It is assigned to a photoproduct denoted with P3 whose structure will be revealed in the following section.

Table 1 presents a list of bands arising from the P1, P2 and P3 photoproducts together with the corresponding theoretical data and the suggested assignment of the product bands.

2.6. Identification of the photoproducts

2.6.1. Photolysed P2T/Ar and P3T/Ar matrices. From the comparison of the positions and intensities of new bands appearing after photolysis with those calculated for the possible photoproducts (see Table S6 in the Supplementary data) it appears that cleavage of the tetrazole ring with the N_2 elimination is a dominating process in the studied P2T/Ar and P3T/Ar matrices. For the 1-substituted tetrazoles P2Ta and P3Ta (P3Tb) studied here the N_2 elimination leads to the formation of pyridin-2-ylcarbodiimide (product P1) or pyridin-3-ylcarbodiimide (product P2). These molecules are characterized by a very intense absorption at 2130.0 (P1) and 2136.0 cm^{-1} (P2) due to the asymmetric stretching mode of the $\text{N}=\text{C}=\text{N}(\text{H})$ moiety, weaker bands at 3423.0 (P1) and 3413.0 cm^{-1} (P2) and 879.0 (P1) and 858.5 cm^{-1} (P2) due to the N–H group stretching and in-plane-deformation modes, respectively. Other bands originating from pyridin-2-ylcarbodiimide and pyridin-3-ylcarbodiimide could also be identified in the spectra of the irradiated samples giving altogether 16 and 17 bands of the product species, respectively, for P1 and P2. The observation of the pyridinylcarbodiimides in the studied matrices is in agreement with the conclusions from previous reports,^{6,7,12,18,21} that have shown 1-substituted tetrazoles to be useful precursors of monosubstituted carbodiimides. To the best of our knowledge the pyridin-2-yl- and pyridin-3-ylcarbodiimides molecules have not been described spectroscopically before. The simplest carbodiimide $\text{HN}=\text{C}=\text{NH}$ was observed as the cyanamide pyrolysis and tetrazole photolysis in argon matrices.^{10,22} Recently, Pagacz-Kostrzewa et al.²³ have shown that both broad-band and narrow-band laser UV irradiations of different isomers of

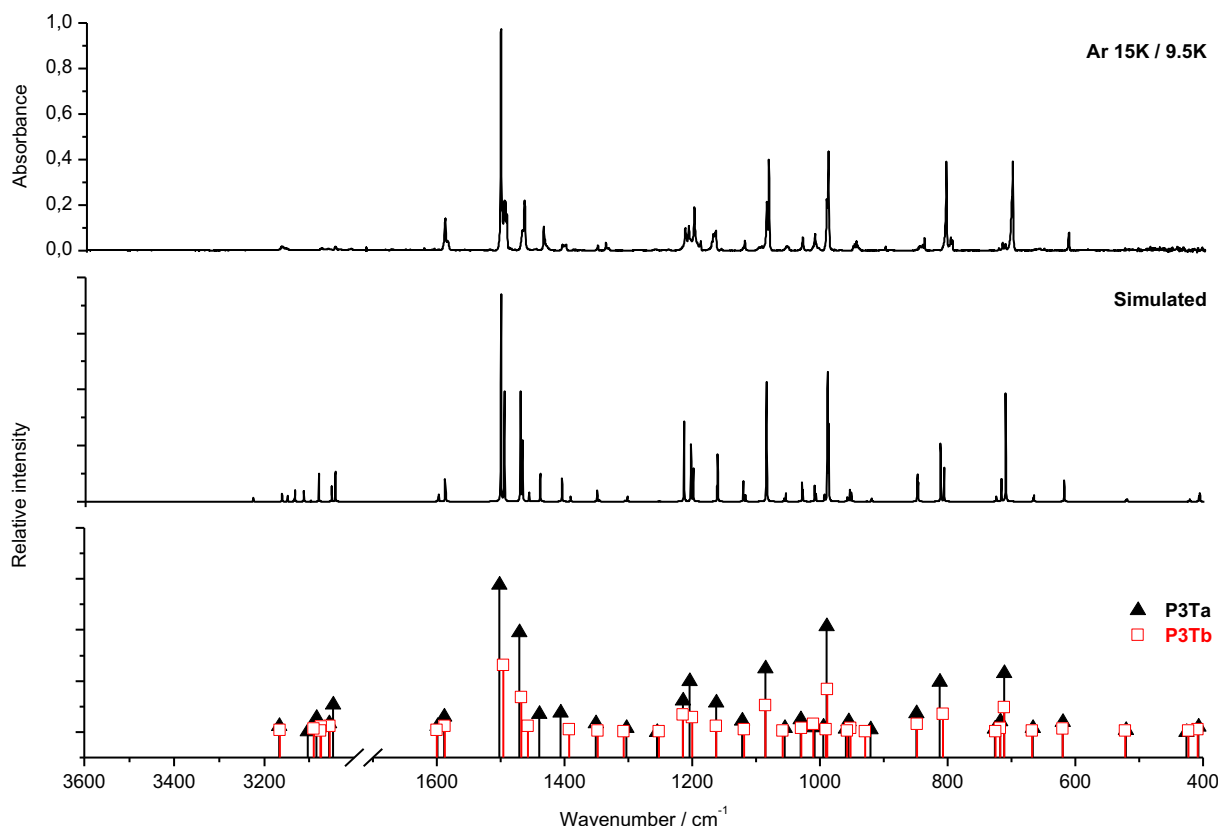


Fig. 8. Infrared spectrum of P3T: *top frame*: spectrum of P3T isolated in Ar matrix, deposition at 15 K, measurement at 9.5 K; *middle frame*: simulated sum spectrum obtained by adding the B3LYP/6-311++G(2d,2p) spectra of the P3Ta and P3Tb conformers weighted by their respective abundances at 333 K (73.77% and 26.23%). The theoretical spectra were created using Lorentzian functions centred at the calculated frequencies scaled as described in [Experimental section](#) and with the bandwidth-at-half-height equal to 0.5 cm⁻¹. *bottom frame*: spectra of P3Ta and P3Tb calculated at the B3LYP/6-311++G(2d,2p) level and scaled by the same scaling factors as for the middle frame.

5-(1*H*-tetrazol-1-yl)-1,2,4-triazole lead to the production of the corresponding 1,2,4-triazolylcarbodiimides.

One possible mechanism of the P1 and P2 formation may involve two concerted bond-breaking processes. According to the ground state calculations performed for the P2Ta and P3Ta precursors the tetrazole ring cleavage might proceed through the weakest, formal single bonds N1–N2 and N3–N4 with lengths of 1.357 and 1.366 Å and 1.360 and 1.362 Å, for P2Ta and P3Ta, respectively. In the course of such reactions 2-(1*H*-diaziren-1-yl)pyridine or 3-(1*H*-diaziren-1-yl)pyridine are expected to be formed as intermediates (see [Table S6 in the Supplementary data](#)).^{7,18,23} The latter species may rearrange in two ways. Both are 1,2-H shifts involving two different N atoms of the diazirene substituent. The first of these pathways leads to the formation of pyridin-2-ylcarbodiimide or pyridin-3-ylcarbodiimide. Indeed these molecules are identified in the studied matrices (P1 and P2). The second possible rearrangement of the (diaziren-1-yl)pyridine intermediates results in formation of the pyridin-2-ylcyanamide or pyrid-3-ylcyanamide species (see [Table S6 in the Supplementary data](#)), which are not observed.

A second possible pathway for the P1 and P2 formation may, as shown by Silva and Bozzelli,²⁴ involve a stepwise mechanism, with initial tetrazolyl ring opening (ring-chain tautomerism) followed by unimolecular bond dissociation. The latter step exhibits a concerted hydrogen shift. It is clearly seen from [Fig. 6](#) that both $S_1 \leftarrow S_0$ and $S_2 \leftarrow S_0$ excitations in P2Ta decrease the electron density between the N1 and N2 atoms. A similar picture is observed for the P3Ta species (see [Figs. S3 in the Supplementary data](#)). Furthermore, the performed TD-DFT calculations reveal that for both P2Ta and P3Ta species, only one of the two weakest, in the S_0 state, bonds of the tetrazole ring

become longer in the first excited state (S_1): the N1–N2 distance increases from 1.352 to 1.392 Å (P2Ta), from 1.361 to 1.386 Å (P3Ta). Thus, the stepwise mechanism analogous to that proposed for 1-*H*-tetrazole²⁴ was considered for the studied compounds to explain the P1 and P2 product formation. Potential energy diagrams for the stepwise dissociation on the S_0 surface of P2Ta and P3Ta are presented in [Fig. 10](#). The products identified in the irradiated P2T/Ar and P3T/Ar matrices (P1 and P2, respectively) indicate that similar, as in [Fig. 10](#), type of reactions may be expected for the photolysed systems.

2.6.2. Photolysed PT/Ar matrices. Comparison of the spectra obtained after the photolysis of the PT/Ar matrices with those obtained for the irradiated P2T/Ar matrices reveals that pyridin-2-ylcarbodiimide (P1) must be one of two main photoproducts appearing in the former matrix as well (see [Fig. 9C](#) and [Table 1](#)). The tetrazolyl ring in the PT1a molecule is bonded to the pyridine ring through the C–C bond contrary to the P2Ta precursor where the C–N bond between the rings is present. Thus, the appearance of the same photoproduct P1 after UV irradiation of both PT1a and P2Ta isolated in argon matrices indicates that, in the case of the PT1a photolysis, a carbon-to-nitrogen rearrangement takes place together with the N₂ elimination from the tetrazolyl ring. Such rearrangement was postulated by Bertrand and Wentrup²⁵ to explain the formation of methylphenylcarbodiimide on flash vacuum thermolysis of 2-methyl-5-phenyltetrazole. Here, to the best of our knowledge, the first spectroscopic evidence for this kind of rearrangement is presented.

[Fig. 11A](#) shows the S_0 potential energy diagram obtained for the PT1a reaction pathway leading to pyridin-2-ylcarbodiimide (P1). A stepwise mechanism for the P1 formation from PT1a is considered

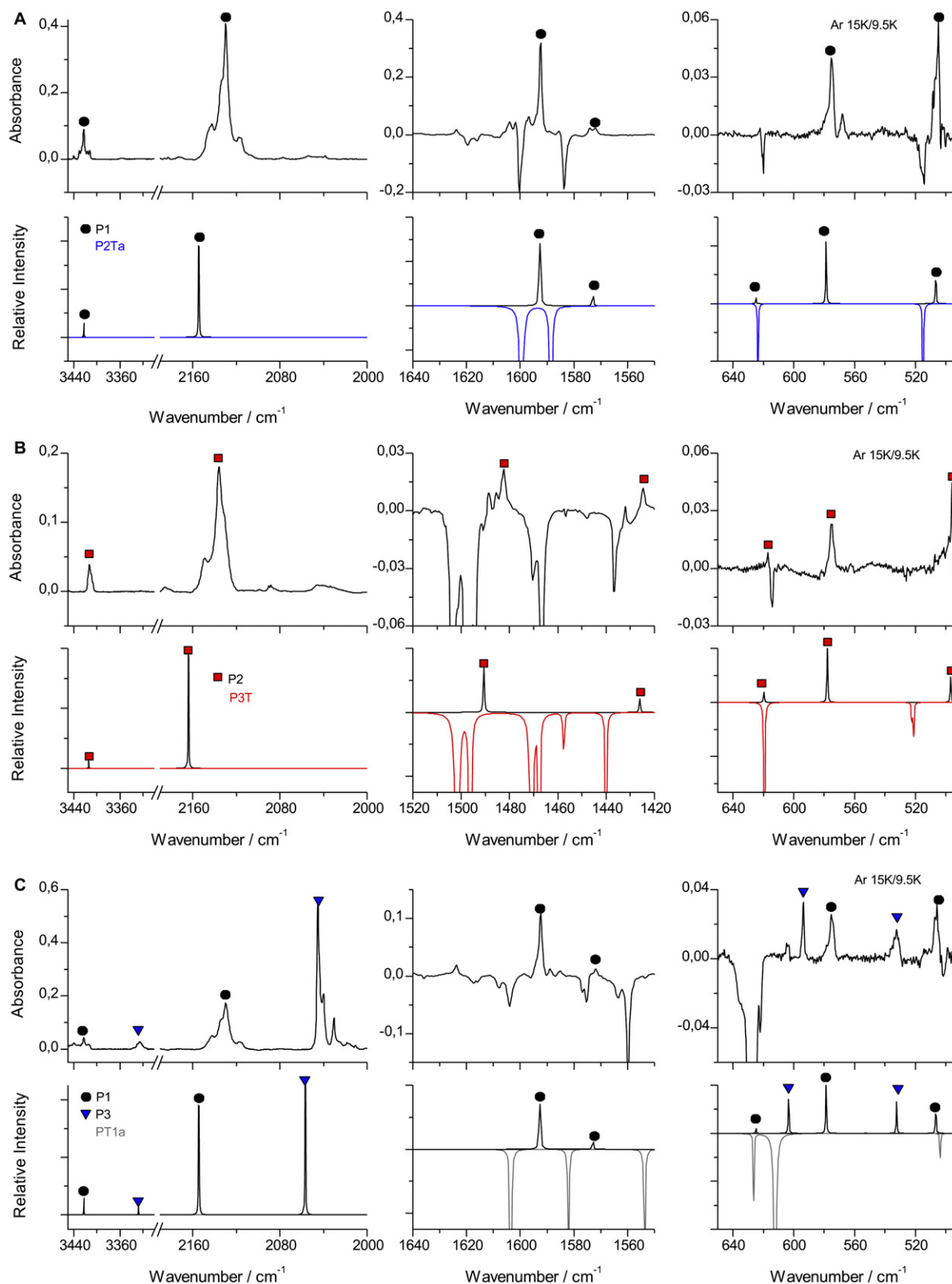
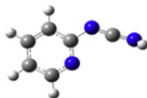
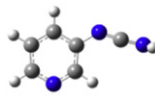
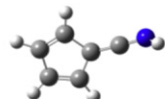


Fig. 9. Selected regions of the spectra. A. *top panel*: experimental difference spectrum of: P2T/Ar after 180 min of irradiation by Xe lamp *minus* freshly deposited P2T/Ar. Growing bands show upward; *bottom panel*: simulated difference spectrum constructed as P1 *minus* P2Ta. Positive bands are due to P1 and negative bands are due to P2Ta. B. *top panel*: experimental difference spectrum of: P3T/Ar after 120 min of irradiation by Xe lamp *minus* freshly deposited P3T/Ar. Growing bands show upward; *bottom panel*: simulated difference spectrum constructed as P2 *minus* (73.77% P3Ta + 26.23% P3Tb). Positive bands are due to P2 and negative bands are due to P3Ta and P3Tb. C. *top panel*: experimental difference spectrum of: PT/Ar after 60 min of irradiation by Xe lamp *minus* freshly deposited PT/Ar. Growing bands show upward. *bottom panel*: simulated difference spectrum constructed as (P1 + P3) *minus* PT1a. Positive bands are due to P1 and P3 and negative bands are due to PT1a.

Table 1

Experimental and calculated harmonic (scaled) frequencies (cm^{-1}) and intensities (k mmol^{-1}) (in parentheses) of the photoproducts observed after photolysis of P2T/Ar, P3T/Ar and PT/Ar matrices

Calculated spectra		Bands observed after photolysis ^a				
ν_{scaled}	ν_{scaled}	ν	I	ν	I	
		P2T/Ar and PT/Ar		P3T/Ar		Assignment
Pyridin-2-yl carbodiimide P1	Pyridin-3-yl carbodiimide P2					
3423 (114)	3414 (105)	3430.5, 3423.0 , 3412.5	w	3416.0, 3413.0 , 3409.5	w	νNH
2154 (1394)	2164 (1411)	2143.0, 2133.5, 2130.0	vs	2149.0, 2136.0 , 2131.0	vs	$\nu_{\text{as}}\text{N}=\text{C}=\text{N}(\text{H})$
1593 (168)	1590 (33)	1592.5	s	1586.5	vw	$\nu\text{CC}(\text{R})+\nu\text{CN}(\text{R})$
1573 (19)	1570 (13)	1572.0	vw	1576.5	vw	$\nu\text{CC}(\text{R})+\nu\text{CN}(\text{R})$
1469 (135)	1491 (61)	1467.5	w	1482.5	vw	$\nu\text{C}-\text{N}+\nu\text{CN}(\text{R})+\delta\text{CH}(\text{R})$
1447 (89)	1426 (18)	1447.0 ^b	vw	1424.5	vw	$\delta\text{CH}(\text{R})+\nu_{\text{s}}\text{N}=\text{C}=\text{N}(\text{H})$
1387 (16)	1395 (5)	1385.0 ^b	vw	1394.0	vw	$\nu_{\text{s}}\text{N}=\text{C}=\text{N}(\text{H})+\delta\text{CH}(\text{R})$
1294 (10)	1338 (1)	1294.0	vw	n.o.		$\delta\text{CH}(\text{R})$
1154 (54)	1132 (38)	1164.5	vw	1131.5	vw	$\delta\text{CCN}(\text{R})+\nu\text{C}-\text{N}$
1148 (17)	1195 (4)	1154.5	vw	n.o.		$\delta\text{CH}(\text{R})$
1094 (2)	1108 (15)	n.o.		1098.5	vw	$\delta\text{CH}(\text{R})$
988 (7)	1019 (10)	n.o.		1023.0	vw	$\delta\text{CC}(\text{R})+\delta\text{CNC}(\text{R})$
871 (446)	884 (440)	879.0	vw	864.5, 858.5	w	δNH
784 (41)	809 (29)	784.0	vw	802.0	vw	$\gamma\text{CH}(\text{R})+\gamma\text{CN}(\text{R})$
739 (20)	708 (30)	738.5	vw	704.0	sh	$\gamma\text{CH}(\text{R})$
670 (34)	655 (34)	674.5	vw	660.5	vw	$\delta\text{N}=\text{C}=\text{N}(\text{H})+\delta\text{CCC}(\text{R})$
625 (4)	620 (8)	n.o.		617.0	vw	$\delta\text{CCC}(\text{R})$
579 (49)	578 (41)	575.0	vw	575.0	vw	τNH
507 (27)	497 (20)	505.0	vw	496.0	w	$\gamma\text{N}=\text{C}=\text{N}(\text{H})+\tau\text{NH}$
ν_{scaled}	ν	I				
	PT/Ar		Assignment		Reference	
1-cyklopenta-2,4-dienylketenimine P3						
3328 (56)	3326.0	vw	νNH	3328 ^c		
2057 (1001)	2045.5 , 2040.0, 2030.5, 2018.5	vs	$\nu_{\text{as}}\text{C}=\text{C}=\text{N}(\text{H})$	2044, 2030, 2017, ^c 2042 ^d		
1462 (73)	1475.0	vw	$\delta\text{CH}+\nu_{\text{s}}\text{C}=\text{C}=\text{N}(\text{H})$			
1398 (30)	1399.0	vw	$\nu_{\text{s}}\text{N}=\text{C}=\text{N}(\text{H})+\nu\text{CC}(\text{R})$			
1320 (1)	1324.5	vw	$\nu\text{CC}(\text{R})+\nu_{\text{s}}\text{C}=\text{C}=\text{N}(\text{H})$			
1176 (1)	1173.0	vw	$\nu\text{CC}(\text{R})+\delta\text{CH}(\text{R})$			
1080 (11)	1083.5	vw	$\delta\text{CH}(\text{R})$			
1075 (3)	1077.0	vw	$\delta\text{CH}(\text{R})$			
916 (367)	859.5	w	δNH			
888 (199)	854.0	vw	$\nu\text{CC}(\text{R})+\delta\text{NH}$			
880 (33)	844.0	vw	$\gamma\text{CH}(\text{R})$			
732 (96)	738.0	vw	$\gamma\text{CH}(\text{R})$			
726 (48)	733.0	w	τNH			
672 (20)	679.0, 677.0	vw	$\gamma\text{CH}(\text{R})+\tau\text{NH}$			
603 (23)	593.5	vw	$\gamma\text{CCC}(\text{R})+\gamma\text{CH}(\text{R})$			
532 (16)	533.5, 532.5 , 530.5	vw	$\gamma\text{CH}(\text{R})+\tau\text{NH}$			
458 (26)	452.5	vw	$\gamma\text{C}=\text{C}=\text{N}(\text{H})$			

Abbreviations: ν —bond stretching, δ —bending, deformation in plane, γ —out-of-plane bending, τ —torsion, R—ring, vs—very strong, v—strong, m—medium, w—weak, vw—very weak.

^a Bold frequencies are the most intense components of the multiplet absorption.

^b Bands not observed in the PT/Ar spectra due to the precursor bands overlapping.

^c Ref. 27.

^d Ref. 26.

leading via a transition state responsible for the carbon-to-nitrogen rearrangement. However, based on the results of the TD-DFT calculations of the electron density changes upon excitation (Fig. S3), the concerted mechanism may not be excluded in this case either.

The results obtained for the PT1a photolysis show that the second reaction pathway, that is, unique for this precursor, occurs in the studied matrices leading to the P3 product characterized by the second set of new bands (see the last part of Table 1). Comparison of the experimental frequencies with a number of the

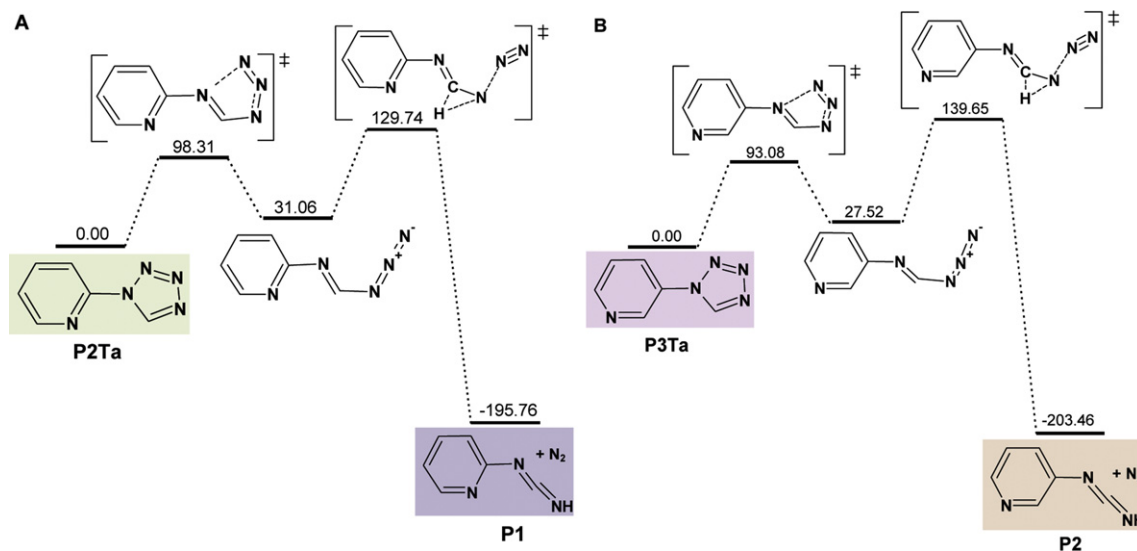


Fig. 10. B3LYP/6-311++G(2d,2p) ZPE corrected potential energy diagram for the stepwise dissociation on the S_0 surface of P2Ta (A) and P3Ta (B) and subsequent P1 and P2 formation. Since the analogous reactions as for P3Ta are expected for the P3Tb conformer the pathways for the latter are not presented. Energies relative to P2Ta (A) or P3Ta (B) in kJ mol^{-1} .

calculated spectra of the possible photoproducts (see Table S6 in the Supplementary data) allowed for the identification of P3 as 1-cyclopenta-2,4-dienylketenimine. This molecule is identified on the basis of 17 bands. Particularly evident is a strong absorption at 2045.5 cm^{-1} due to the asymmetric stretching mode of the $\text{C}=\text{C}=\text{N}(\text{H})$ fragment and a weaker band at 3326.0 cm^{-1} assigned to the ν NH stretch. The ketenimine molecule was identified by Tomioka et al.²⁶ after (2-nitrophenyl)diazomethane photolysis and by Kiszka et al.²⁷ as one of the minor products of the benzotriazole photolysis in low temperature matrices. Positions of the IR bands reported by these authors are given in Table 1 for comparison.

The calculated S_0 potential energy diagram showing a possible transformation leading to the 1-cyclopenta-2,4-dienylketenimine formation is presented in Fig. 11B. The suggested pathway starts with the elimination of two N_2 molecules, through a series of intermediates leading to the final product 1-cyclopenta-2,4-dienylketenimine (P3). This diagram, in some points similar to that proposed for the 3-pyridazincarbene-2-pyridylnitrene rearrangement by Wentrup,²⁸ contains pyridylcarbene and pyridylnitrene both in their singlet states. The latter species undergoes further reactions through two high energy transition states forming 1-cyclopenta-2,4-dienylketenimine (P3) as the final product. The latter species was reported by Yranzo et al.²¹ as an unstable intermediate formed during flash vacuum thermolysis of the isatin derivative, which tautomerized to cyanocyclopentadiene. However, at the matrix isolation conditions this ketenimine (P3) remained stable and could be detected.

It is worth noting that both P1 (pyridin-2-ylcarbodiimide) and P2 (pyridin-3-ylcarbodiimide) photoproducts may appear as two conformers differing in positions of the NCNH moiety relative to the N-atom of the pyridine ring. Fig. 12 shows the potential energy diagram for the P1 and P2 products. The higher energy conformers of P1 and P2 are denoted as P1' and P2', respectively. It is clear from this figure that if both conformers of P1 and P2 are produced in the irradiated matrices, the less stable species must isomerize to their lower energy counterpart, similarly to that reported for 1H-1,2,4-triazol-5-ylcarbodiimide and 1H-1,2,4-triazol-3-ylcarbodiimide.²³ Such a process is justified by the low values of the calculated energy barriers for the P1' \rightarrow P1 and P2' \rightarrow P2 conversion equal to 2.53 and 7.37 kJ mol^{-1} , respectively. This conclusion is also in agreement with the experimental

findings since only the more stable conformer from each pair was detected in the present experiment.

2.6.3. Other photolysis products. There are several very weak absorptions appearing in the spectra of the irradiated P3T/Ar matrices, which are still not assigned. The most characteristic among them are weak multiple bands found in the $3330\text{--}3120 \text{ cm}^{-1}$ range in the spectra after the P3T/Ar matrices photolysis (see Fig. S4 in the Supplementary data). They are attributed to the presence of HCN associated to other species formed in the same matrix cage.^{23,29}

3. Conclusion

Among three tetrazolypyridines studied by means of the infrared matrix isolation spectroscopy, 2-(tetrazol-1-yl)pyridine (P2T) and 2-(tetrazol-5-yl)pyridine (PT) were found to exist in one most stable form (P2Ta and PT1a, respectively) while two conformers of 3-(tetrazol-5-yl)pyridine (P3Ta and P3Tb) were identified in solid argon. These observations are in good agreement with the B3LYP/6-311++G(2d,2p) predictions.

Broad-band irradiation of the P2Ta, P3Ta/P3Tb and PT1a species isolated in argon matrices led to cleavage of the tetrazole ring with the N_2 elimination observed for each of the studied species with the simultaneous formation of pyridin-2-ylcarbodiimide (product P1) or pyridin-3-ylcarbodiimide (product P2). In spite of the different structure of the P2Ta and PT1a precursors, the same photoproduct P1 was detected for both species indicating that a carbon-to-nitrogen rearrangement took place in the case of the PT1a molecule. Spectroscopic evidence of this process supported by the results of quantum chemical calculations is presented.

An additional, unique for the PT1a precursor, reaction pathway was found consisting in two N_2 molecules elimination and leading to 1-cyclopenta-2,4-dienylketenimine (P3) as a final photoproduct.

4. Experimental

4.1. Synthesis and analysis of the compounds

2-(Tetrazol-1-yl)pyridine, 3-(tetrazol-1-yl)pyridine and 2-(tetrazol-5-yl)pyridine were prepared according to the known

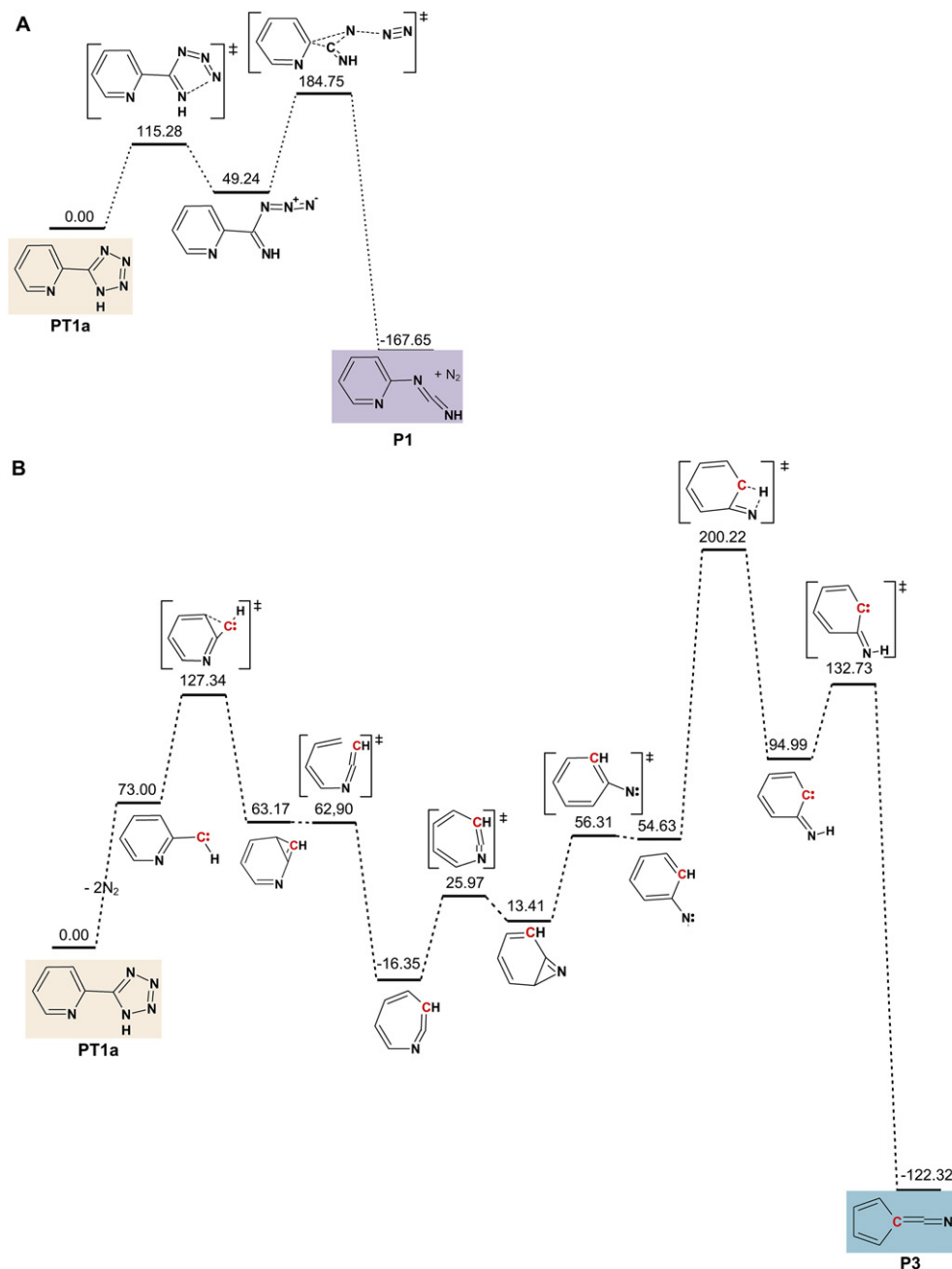


Fig. 11. B3LYP/6-311++G(2d,2p) ZPE corrected S_0 potential energy diagrams: A. for the stepwise dissociation of PT1a leading to the P1 formation; B. the reaction pathway leading to the P3 product. Energies relative to PT1a in kJ mol^{-1} . For all species in scheme B but PT1a the energy values shown contain the two N_2 molecules contribution.

procedures.^{14,30,31} Calc. for $\text{C}_6\text{H}_5\text{N}_5$: C, 49.0; H, 3.4; N, 47.6%. Anal. found ($M_w=147.14$), P2T: C, 48.9; H, 3.2; N, 47.8%; P3T: C, 49.0; H, 3.2; N, 47.6%; PT: C, 49.1; H, 3.3; N, 47.7%.

P2T δ_{H} (600 MHz, CDCl_3 , 298 K) 9.48 (1H, s), 8.49 (1H, ddd, J 4.9, 1.5, 0.7 Hz), 8.04 (1H, dt, J 8.2, 0.8 Hz), 7.93 (1H, td, J 7.9, 1.8 Hz), 7.39 (1H, ddd, J 7.5, 4.8, 1.0 Hz); δ_{C} (300 MHz, CDCl_3 , 298 K): 149.1, 146.9, 140.1, 139.8, 124.8, 114.4. P3T δ_{H} (300 MHz, CD_3CN , 298 K) 9.40 (1H, s), 9.02 (1H, dd, J 2.4, 0.3 Hz), 8.75 (1H, dd, J 4.8, 1.3 Hz), 8.17 (1H, ddd, J 8.3, 2.6, 1.4 Hz), 7.62 (1H, ddd, J 8.3, 4.8, 0.8 Hz); δ_{C} (300 MHz, CD_3CN , 298 K): 152.3, 144.0, 143.4, 132.5, 130.6, 125.9. PT: δ_{H} (600 MHz, $\text{DMSO}-d_6$, 298 K) 8.86 (1H, ddd, J 4.8, 1.7, 1.0 Hz), 8.29 (1H, dt, J 7.9, 1.0 Hz), 8.14 (1H, td, J 7.8, 1.7 Hz), 7.70 (1H, ddd, J 7.6, 4.8, 1.1 Hz); δ_{C} (600 MHz, $\text{DMSO}-d_6$, 298 K): 154.8, 150.1, 143.6, 138.2, 126.1, 122.6.

4.2. Computational details

All ground state calculations were performed with the Gaussian 09 programs package.³² Structures of the minima have been optimized at the B3LYP level with the 6-311++G(2d,2p) basis set. The associated force constant matrixes were calculated to evaluate harmonic frequencies and zero-point vibrational (ZPE) corrections. The DFT calculated frequencies were scaled to account for anharmonicity effects: above 2000 cm^{-1} by 0.960, 0.963, 0.951 or 0.949 and between 2000 and 500 cm^{-1} by 0.980, 0.983, 0.982 and 0.979 for P2T, P3T, PT and photoproducts, respectively. Potential energy distributions (PED) of the normal modes were computed with the GAR2PED program³³ and the vibrational spectra were simulated using SYNSPEC program.³⁴ Geometry of the first excited states and

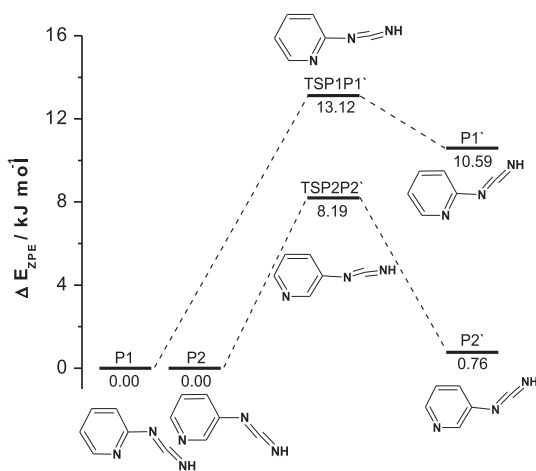


Fig. 12. B3LYP/6-311++G(2d,2p) ZPE corrected potential energy diagram for the P1 and P2 isomerizations. Energy of P1' and P2' in kJ mol^{-1} relative to P1 and P2, respectively.

the vertical excitation energies were calculated using the time-dependent functional theory TD-DFT^{35,36} implemented in the Turbomole³⁷ program package.

4.3. Infrared spectra and photolysis

The crystalline sample of the studied compounds was placed in a small electric oven assembled inside the cryostat. The temperature of the oven was controlled by the DC regulated power supply (NDN Instruments) that allowed for the precise regulation of the current. Matrices were prepared by co-deposition of P2T, P3T or PT vapours coming out of the oven with large excess of argon onto the cold CsI window. The low temperature was maintained by means of a closed cycle helium refrigerator (ARS-2HW). FTIR spectra were recorded between 4000–400 cm^{-1} in a transmission mode by means of a Bruker 66 FTIR spectrometer with a resolution of 0.5 cm^{-1} and using a liquid N_2 cooled MCT detector.

After the infrared spectra of the initially deposited matrices were recorded the samples were irradiated with a 450 W output power of a Xe lamp (Optel ZXE-450) for up to 240 min. The lamp was fitted with a 5 cm water filter and a series of long-pass optical filters (Schott WG: 435, 394, 345, 320, 305, 295 and 280 nm).

Acknowledgements

A grant of computer time from the Wrocław Center for Networking and Supercomputing is gratefully acknowledged. Mr. M.G. Dąbrowski is thanked for his contribution during preliminary experiments on P2T.

Supplementary data

Geometry of the P2T, P3T and PT conformers and transition states optimized at the B3LYP/6-311++G(2d,2p) level (Table S1), energetics, abundances, key dihedral angles and dipole moments for P2T, P3T and PT isomers and transition states calculated at the B3LYP/6-311++G(2d,2p) level (Table S2), S_1 excited state geometry parameters and their changes as compared with S_0 state (Table S3), experimental and calculated frequencies and intensities for P2Ta, P3Ta and P3Tb and PT1a (Table S4), definition of internal coordinates and normal coordinate analysis for P2Ta, P3Ta, P3Tb and PT conformers (Table S5), B3LYP/6-311++G(2d,2p) calculated frequencies and intensities of the possible photoproducts (Table S6), optimized structures of the high energy PT isomers (Fig. S1),

optimized structures of the transition states linking PT isomers (Fig. S2), density differences calculated at the P3Ta and PT1a ground state, between S_1 and S_0 and S_2 and S_0 (Fig. S3), HCN stretching region in the experimental spectrum of the irradiated P3T/Ar matrix (Fig. S4). Supplementary data associated with this article can be found, in the online version, at doi:10.1016/j.tet.2011.08.055.

References and notes

- Gaponik, P. N.; Voitekhovich, S. V.; Ivashkevich, O. A. *Russ. Chem. Rev.* **2006**, *75*, 507–539.
- Stierstorfer, J.; Tarantik, K. R.; Klapötke, T. M. *Chem.—Eur. J.* **2009**, *15*, 5775–5792.
- Myznikov, L. V.; Hrabalek, A.; Koldobskii, G. I. *Chem. Heterocycl. Compd.* **2007**, *43*, 1–9.
- Herr, R. J. *Bioorg. Med. Chem.* **2002**, *10*, 3379–3393.
- May, B. C. H.; Abell, A. D. J. *Chem. Soc., Perkin Trans. 1* **2002**, 172–178.
- Gómez-Zavaglia, A.; Reva, I. D.; Frija, L.; Cristiano, M. L.; Fausto, R. J. *Photochem. Photobiol., A* **2006**, *179*, 243–255.
- Gómez-Zavaglia, A.; Reva, I. D.; Frija, L.; Cristiano, M. L.; Fausto, R. J. *Mol. Struct.* **2006**, *786*, 182–192.
- Frija, L.; Reva, I. D.; Gómez-Zavaglia, A.; Cristiano, M. L.; Fausto, R. J. *Phys. Chem. A* **2007**, *111*, 2879–2888.
- Pagacz-Kostrzewa, M.; Białońska, A.; Bronisz, R.; Wierzejewska, M. J. *Mol. Struct.* **2010**, *976*, 431–439.
- Maier, G.; Eckert, J.; Bothur, A.; Reisenauer, H. P.; Schmidt, C. *Liebigs Ann.* **1996**, 1041–1053.
- Grimshaw, J. In *CRC Handbook of Organic Photochemistry and Photobiology*; Horspool, W. W. M., Lenci, F., Eds.; CRC LLC: Boca Raton, FL, 2004; Chapter 43, pp 1–17.
- Frija, L. M.; Ismael, A.; Cristino, M. L. S. *Molecules* **2010**, *15*, 3757–3774.
- Frija, A.; Khmelinskii, I. V.; Serpa, C.; Reva, I. D.; Fausto, R.; Cristino, M. L. S. *Org. Biomol. Chem.* **2008**, *6*, 1046–1055.
- Grunert, C. M.; Weinberger, P.; Schweifer, J.; Hampel, Ch.; Stassen, A. F.; Meier, K.; Linert, W. J. *Mol. Struct.* **2005**, *733*, 41–52.
- Rizk, A. T.; Kilner, C. A.; Halcrow, M. A. *CrystEngComm* **2005**, *7*, 359–362.
- Addicott, C.; Wong, M. W.; Wentrup, C. J. *Org. Chem.* **2002**, *67*, 8538–8546.
- Addicott, C.; Reisinger, A.; Wentrup, C. J. *Org. Chem.* **2003**, *68*, 1470–1474.
- Gómez-Zavaglia, A.; Reva, I. D.; Frija, L.; Cristiano, M. L.; Fausto, R. J. *Phys. Chem. A* **2005**, *109*, 7967–7976.
- Ismael, A.; Cristiano, M. L. S.; Fausto, R.; Gómez-Zavaglia, A. J. *Phys. Chem. A* **2010**, *114*, 13076–13085.
- Kvaskoff, D.; Bednarek, P.; Wentrup, C. J. *Org. Chem.* **2010**, *75*, 1600–1611.
- Yranzo, G. I.; Elguero, J.; Flammang, R.; Wentrup, C. *Eur. J. Org. Chem.* **2001**, *12*, 2209–2220.
- King, S. T.; Strope, J. H. J. *Chem. Phys.* **1971**, *54*, 1289–1295.
- Pagacz-Kostrzewa, M.; Reva, I. D.; Bronisz, R.; Giuliano, B. M.; Fausto, R.; Wierzejewska, M. J. *Phys. Chem. A* **2011**, *115*, 5693–5707.
- da Silva, G.; Bozzelli, J. W. J. *Org. Chem.* **2008**, *73*, 1343–1353.
- Bertrand, G.; Wentrup, C. *Angew. Chem., Int. Ed. Engl.* **1994**, *33*, 527–545.
- Tomioka, H.; Ichikawa, N.; Komatsu, K. J. *Am. Chem. Soc.* **1992**, *114*, 8045–8053.
- Kiszka, M.; Dunkin, I. R.; Gębicki, J.; Wang, H.; Wirz, J. J. *Chem. Soc., Perkin Trans. 2* **2000**, 2420–2426.
- Wentrup, C. *Acc. Chem. Res.* **2011**, *44*, 393–404.
- Langel, W.; Kollhoff, H.; Knözinger, E. J. *Chem. Phys.* **1989**, *90*, 3430–3442.
- Denton, T. T.; Zhang, X.; Cashman, J. R. J. *Med. Chem.* **2005**, *48*, 224–239.
- Finnegan, W. G.; Henry, R. A.; Lofquist, R. J. *Am. Chem. Soc.* **1958**, *80*, 3908–3911.
- Frisch, M. J.; Trucks, G. W.; Schlegel, H. B.; Scuseria, G. E.; Robb, M. A.; Cheeseman, J. R.; Scalmani, G.; Barone, V.; Mennucci, B.; Petersson, G. A.; Nakatsuji, H.; Caricato, M.; Li, X.; Hratchian, H. P.; Izmaylov, A. F.; Bloino, J.; Zheng, G.; Sonnenberg, J. L.; Hada, M.; Ehara, M.; Toyota, K.; Fukuda, R.; Hasegawa, J.; Ishida, M.; Nakajima, T.; Honda, Y.; Kitao, O.; Nakai, H.; Vreven, T.; Montgomery, J. A., Jr.; Peralta, J. E.; Ogliaro, F.; Bearpark, M.; Heyd, J. J.; Brothers, E.; Kudin, K. N.; Staroverov, V. N.; Kobayashi, R.; Normand, J.; Raghavachari, K.; Rendell, A.; Burant, J. C.; Iyengar, S. S.; Tomasi, J.; Cossi, M.; Rega, N.; Millam, N. J.; Klene, M.; Knox, J. E.; Cross, J. B.; Bakken, V.; Adamo, C.; Jaramillo, J.; Gomperts, R.; Stratmann, R. E.; Yazyev, O.; Austin, A. J.; Cammi, R.; Pomelli, C.; Ochterski, J. W.; Martin, R. L.; Morokuma, K.; Zakrzewski, V. G.; Voth, G. A.; Salvador, P.; Dannenberg, J. J.; Dapprich, S.; Daniels, A. D.; Farkas, Ö.; Foresman, J. B.; Ortiz, J. V.; Cioslowski, J.; Fox, D. J. *Gaussian 09, Revision A.02*; Gaussian: Wallingford CT, 2009.
- Martin, J. M. L.; Van Alsenoy, C. *GAR2PED*; University of Antwerp: Antwerpen, Belgium, 1995.
- Irikura, K. In *Multiphoton absorption strengths from simple ab initio wavefunctions*; National Institute of Standards and Technology: Gaithersburg, MD 20899, USA, 1995.
- Bauernschmitt, R.; Ahlrichs, R. *Chem. Phys. Lett.* **1996**, *256*, 454–464.
- Stratmann, R. E.; Scuseria, G. E.; Frisch, M. J. *Chem. Phys.* **1998**, *109*, 8218–8224.
- See: <http://www.turbomole.com> for TURBOMOLE V6, 2 2010, a development of University of Karlsruhe and Forschungszentrum Karlsruhe GmbH, 1989–2007, TURBOMOLE GmbH, since 2007.